VERITAS Discovery of VHE Emission from the Radio Galaxy 3C 264: A Multiwavelength Study

A. Archer[1], W. Benbow[2], R. Bird[3], A. Brill[4], M. Buchovecky[3], J. H. Buckley[5], M. T. Carini[6], J. L. Christiansen[7], A. J. Chromey[8], M. K. Daniel[2], M. Errando[5], A. Falcone[9], Q. Feng[4], P. Fortin[2], L. Fortson[10], A. Furniss[11], A. Gent[12], M. Georganopoulos[13], G. H. Gillanders[14], C. Giuri[15], O. Gueta[15], D. Hanna[16], T. Hassan[15], O. Hervet[17], J. Holder[18], G. Hughes[2], T. B. Humensky[4], P. Kaaret[19], M. Kertzman[1], D. Kieda[20], F. Krennrich[8], M. J. Lang[14], T. T. Y. Lin[16], M. L. Lister[21], M. Lundy[16], G. Maier[15], E. Meyer[13], P. Moriarty[14], R. Mukherjee[22], D. Nieto[23], M. Nievas-Rosillo[15], S. O'Brien[16], R. A. Ong[3], K. Pfrang[15], M. Pohl[24], R. R. Prado[15], E. Pueschel[15], J. Quinn[25], K. Ragan[16], K. Ramirez[7], P. T. Reynolds[26], D. Ribeiro[4], G. T. Richards[18], E. Roache[2], C. Rulten[10], J. L. Ryan[3], A. Sadun[27], M. Santander[28], S. S. Scott[17], G. H. Sembroski[29], K. Shahinyan[10], R. Shang[3], B. Stevenson[3], V. V. Vassiliev[3], S. P. Wakely[30], A. Weinstein[8], P. Wilcox[10], A. Wilhelm[24], D. A. Williams[17], and T. J Williamson[18]

[1] Department of Physics and Astronomy, DePauw University, Greencastle, IN 46135-0037, USA
[2] Center for Astrophysics | Harvard & Smithsonian, Cambridge, MA 02138, USA; wbenbow@cfa.harvard.edu
[3] Department of Physics and Astronomy, University of California, Los Angeles, CA 90095, USA
[4] Physics Department, Columbia University, New York, NY 10027, USA
[5] Department of Physics, Washington University, St. Louis, MO 63130, USA
[6] Department of Physics and Astronomy | Western Kentucky University, Bowling Green, KY 42103, USA
[7] Physics Department, California Polytechnic State University, San Luis Obispo, CA 94307, USA; jlchrist@calpoly.edu
[8] Department of Physics and Astronomy, Iowa State University, Ames, IA 50011, USA
[9] Department of Astronomy and Astrophysics, 525 Davey Lab, Pennsylvania State University, University Park, PA 16802, USA
[10] School of Physics and Astronomy, University of Minnesota, Minneapolis, MN 55455, USA; lfortson@umn.edu
[11] Department of Physics, California State University—East Bay, Hayward, CA 94542, USA
[12] School of Physics and Center for Relativistic Astrophysics, Georgia Institute of Technology, 837 State Street NW, Atlanta, GA 30332-0430, USA
[13] Department of Physics, University of Maryland, Baltimore County, Baltimore, MD 21250, USA; georgano@umbc.edu, meyer@umbc.edu
[14] School of Physics, National University of Ireland Galway, University Road, Galway, Ireland
[15] DESY, Platanenallee 6, D-15738 Zeuthen, Germany
[16] Physics Department, McGill University, Montreal, QC H3A 2T8, Canada
[17] Santa Cruz Institute for Particle Physics and Department of Physics, University of California, Santa Cruz, CA 95064, USA
[18] Department of Physics and Astronomy and the Bartol Research Institute, University of Delaware, Newark, DE 19716, USA
[19] Department of Physics and Astronomy, University of Iowa, Van Allen Hall, Iowa City, IA 52242, USA
[20] Department of Physics and Astronomy, University of Utah, Salt Lake City, UT 84112, USA
[21] Department of Physics and Astronomy, Purdue University, 525 Northwestern Avenue, West Lafayette, IN 47907, USA; mlister@purdue.edu
[22] Department of Physics and Astronomy, Barnard College, Columbia University, NY 10027, USA
[23] Institute of Particle and Cosmos Physics, Universidad Complutense de Madrid, E-28040 Madrid, Spain
[24] Institute of Physics and Astronomy, University of Potsdam, 14476 Potsdam-Golm, Germany and DESY, Platanenallee 6, D-15738 Zeuthen, Germany
[25] School of Physics, University College Dublin, Belfield, Dublin 4, Ireland
[26] Department of Physical Sciences, Cork Institute of Technology, Bishopstown, Cork, Ireland
[27] Department of Physics | University of Colorado Denver, Denver, CO 80217, USA
[28] Department of Physics and Astronomy, University of Alabama, Tuscaloosa, AL 35487, USA
[29] Department of Physics and Astronomy, Purdue University, West Lafayette, IN 47907, USA
[30] Enrico Fermi Institute, University of Chicago, Chicago, IL 60637, USA

Abstract

The radio source 3C 264, hosted by the giant elliptical galaxy NGC 3862, was observed with the Very Energetic Radiation Imaging Telescope Array System (VERITAS) between 2017 February and 2019 May. These deep observations resulted in the discovery of very high energy (VHE; $E > 100$ GeV) γ-ray emission from this active galaxy. An analysis of $\sim$57 hr of quality-selected live time yields a detection at the position of the source, corresponding to a statistical significance of 7.8 standard deviations above background. The observed VHE flux is variable on monthly timescales, with an elevated flux seen in 2018 observations. The VHE emission during this elevated state is well characterized by a power-law spectrum with a photon index $\Gamma = 2.20 \pm 0.27$ and flux $F(>315 \text{ GeV}) = (7.6 \pm 1.2_{\text{stat}} \pm 2.3_{\text{syst}}) \times 10^{-13} \text{ cm}^{-2} \text{ s}^{-1}$, or approximately 0.7% of the Crab Nebula flux above the same threshold. 3C 264 ($z = 0.0217$) is the most distant radio galaxy detected at VHE, and the elevated state is thought to be similar to that of the famously outbursting jet in M87. Consequently, extensive contemporaneous multiwavelength data were acquired in 2018 at the time of the VHE high state. An analysis of these data, including Very Long Baseline Array, Very Large Array, Hubble Space Telescope, Chandra, and Swift observations in addition to the VERITAS data, is presented, along with a discussion of the resulting spectral energy distribution.

1. Introduction

Active galactic nuclei (AGNs) constitute a small fraction of supermassive black holes at the centers of galaxies. These objects are powered by accretion, and a further fraction (∼10%) of AGNs have highly collimated jets of fully ionized plasma that can reach scales of several megaparsecs. Numerous AGNs are known to emit high-energy (HE; MeV−GeV) and very high energy (VHE; $E > 100$ GeV) γ-rays, presumably via inverse Compton (IC) emission of leptonic particles within the jet. All but four of the 78 (jetted) AGNs currently detected at VHE are blazars, where the jet is viewed nearly along its axis; the other four are radio galaxies where the jet associated with the AGN is viewed at somewhat larger angles.[31] It has been suggested that radio galaxies form the parent population of blazars with core-dominated objects (FR I galaxies, after the Fanaroff & Riley 1974 classification) corresponding to BL Lac objects observed at larger jet viewing angles, while lobe-dominated FR II radio galaxies are, instead, associated with flat-spectrum radio quasars (Urry & Padovani 1995).

The jet emission in blazars and radio galaxies is characterized by a double-peaked, nonthermal spectral energy distribution (SED). The lower-frequency peak, which in blazars has a peak frequency (ν_{peak}) ranging from 10^{13} to 10^{18} Hz, is well described as synchrotron emission from relativistic electrons spiraling in the magnetic field of the jet. The higher-frequency peak, located in the γ-ray band, is generally attributed to IC emission. Typically, the sources with higher-frequency synchrotron peaks have higher-frequency IC peaks (i.e., beyond the 10−100 GeV range). Correspondingly, high-synchrotron-peaked (HSP) blazars ($\nu_{peak} > 10^{15}$ Hz) are the brightest and best-studied AGNs at VHE (51 of the current VHE AGNs), even though they are the least luminous/powerful. In contrast, only nine blazars (BL Lac objects and quasars) in the current TeV catalog are low-synchrotron-peaked (LSP; $\nu_{peak} \lesssim 10^{14}$ Hz) objects. Although there is no strict division between the classes, radio galaxies are believed to have their jets oriented at larger angles to the line of sight ($\gtrsim 10°$) than blazars. This larger misalignment means that radio galaxies are much less Doppler boosted than their blazar counterparts and that they tend to have lower-frequency synchrotron peaks, similar to LSP blazars (Meyer et al. 2011).

The IC emission in blazars and radio galaxies can arise from synchrotron self-Compton (SSC) or external Compton processes, or a combination of the two. It is generally thought that most low-power blazars (i.e., HSPs) have IC peaks dominated by SSC emission (e.g., Böttcher 2007; Paggi et al. 2009), while the more powerful blazars (i.e., LSPs) are likely to require external Compton processes (Sikora et al. 2009; Meyer et al. 2012). In the latter case, it is unclear which external photon field provides the seed photons for scattering, due to the uncertainty in the actual location of the HE emitting region in the jet (e.g., Arsioli & Chang 2018). The possibilities for the dominant seed-photon source include the molecular torus region, the much smaller broad-line-emitting region, and even the accretion disk (Dermer et al. 1992; Sikora et al. 1994; Błażejowski et al. 2000; Sikora et al. 2009). In addition to these purely leptonic scenarios, there are also models for jet emission that include a significant population of relativistic protons (i.e., hadronic models) that produce HE and VHE γ-ray emission via several different processes (e.g., Aharonian 2000). In

particular, cloud−jet interaction models could explain the observed teraelectronvolt flaring emission in sources like M87 (e.g., Barkov et al. 2012).

This paper describes the discovery by Very Energetic Radiation Imaging Telescope Array System (VERITAS) in VHE γ-rays of the FR I radio galaxy 3C 264. It is the fourth radio galaxy detected at VHE, and the most distant, at a comoving distance of 93 Mpc. All four VHE radio galaxies are low-power, with FR I type jets. The other VHE detections are Centaurus A, M87, and NGC 1275 (at a distance of 3.8, 16.7, and 62.5 Mpc, respectively; Blakeslee et al. 2009; Harris et al. 2010; Tully et al. 2013). Two of the four VHE radio galaxies show superluminal motions on kiloparsec scales (3C 264 and M87). It is plausible that some very nearby radio galaxies are designated such because their proximity makes the identification of their host galaxy easier. At much larger distances, the same objects would likely be classified as (slightly misaligned) blazars. Indeed, the VHE source IC 310, detected by both VERITAS and MAGIC (Aleksić et al. 2014), is considered by some to be a fifth VHE radio galaxy (Feretti et al. 1998; Sijbring & de Bruyn 1998). However, there are convincing arguments that it is a borderline BL Lac object (Kadler et al. 2012). A similar case is the VHE source PKS 0625−354, for which there is also some ambiguity, although the balance of evidence is in favor of a BL Lac classification (HESS Collaboration et al. 2018).

Previous VHE detections of radio galaxies reveal HE Compton components similar to blazars in terms of spectral shape and origin, though at lower luminosity owing to the decreased Doppler boosting. As is sometimes the case for blazars, single-zone SSC models are usually inadequate to explain the observed emission. In the blazar/radio galaxy IC 310, a rising TeV component led to suggestions for a hadronic origin, or a leptonic origin with multiple electron distributions (Fraija et al. 2017). A similar spectral hardening at VHE is seen in Cen A (Aharonian et al. 2009) and possibly M87 (Rieger & Levinson 2018). In contrast, a single-zone SSC model is compatible with the HE emission and variability of NGC 1275 (Aleksić et al. 2014).

Comparing jet structure within VHE radio galaxies, 3C 264 closely resembles M87. Both have one-sided FR I type jets with the same kinetic luminosity ($10^{43.8}$ erg s^{-1}; Meyer et al. 2011). Their jets also have similar morphological traits (i.e., multiple knots), and they share similar qualitative kinematic characteristics within the jet substructure (Meyer et al. 2015). In contrast, NGC 1275 and Cen A both have misaligned two-sided radio jets. M87 has famously shown an outburst in the optical and X-ray bands from HST-1, a knot ∼100 pc downstream of the core (sky-projected; Harris et al. 2006). It has also exhibited extreme (day-scale) VHE variability on multiple occasions (Aharonian et al. 2006; Harris et al. 2009; Aliu et al. 2012), which some attribute to HST-1, rather than the core. In light of the similarities between M87 and 3C 264, and due to the ongoing collision between two knots in the 3C 264 jet (Meyer et al. 2015), a suite of contemporaneous multiwavelength observations was assembled to complement the detection of an increased VHE flux from 3C 264 in early 2018. The goal was to observe a change in brightness or structure within the jet or core during the same period. Therefore, in addition to the VERITAS VHE discovery of 3C 264, this paper describes the results from this multiwavelength observation campaign, as well as the similarities and

---

[31] TeVCat online source catalog: Wakely & Horan (2008).

Table 1
Results from VERITAS Observations of 3C 264 in 2017−2019

Epoch	MJD	T (hr)	On	Off	Normalization	Excess	Significance (σ)	Flux (>315 GeV) (10^{-13} cm^{-2} s^{-1})	Crab (%)
Total (2017–2019)	57811−58633	57.0	225	1856	0.0666	101.4	7.8	5.8 ± 0.9	0.54 ± 0.08
2017 Feb–May	57811−57893	9.2	26	306	0.0663	5.7	1.2	1.9 ± 1.7	0.18 ± 0.16
2018 Feb–April	58158−58229	37.9	172	1279	0.0665	87.0	7.9	7.6 ± 1.2	0.71 ± 0.11
2019 Jan–May	58487−58633	10.0	27	271	0.0674	8.8	1.8	2.9 ± 1.8	0.27 ± 0.17
2018 Feb	58158−58170	3.0	20	102	0.0667	13.2	3.9	13.1 ± 4.5	1.20 ± 0.41
2018 Mar	58186−58198	17.7	93	599	0.0667	53.0	6.8	10.2 ± 1.9	0.95 ± 0.18
2018 Apr	58212−58229	17.2	59	578	0.0662	20.8	3.0	4.0 ± 1.5	0.37 ± 0.14

Note. The quality-selected live time, the number of γ-ray-like events in the on- and off-source regions, the normalization for the larger off-source region, the observed excess of γ-rays, and the corresponding statistical significance are shown. For each observation epoch, the integral flux corresponding to the observed excess is given. For the 2017 and 2019 observations, an upper limit may be more appropriate, and this information is given in the text. The flux is reported above the observation threshold of 315 GeV and is also given in percentage of Crab Nebula flux above the same threshold. Some quantities may not appear to sum precisely as a result of rounding.

differences between 3C 264 and M87, particularly in light of their variability on 100–1000 pc scales and at VHE.

In this paper a standard ΛCDM cosmology is assumed with $H_0 = 67.8$ km s^{-1} Mpc^{-1}, $\Omega_M = 0.308$, and $\Omega_\Lambda = 0.692$. The luminosity distances to 3C 264 and M87 are 95.4 and 22.2 Mpc, respectively.

2. VERITAS Data and Results

The VERITAS is an array of four imaging atmospheric Cerenkov telescopes located at Fred Lawrence Whipple Observatory near Amado, Arizona (31° 40'N, 110° 57'W). The 12 m diameter telescopes are of the Davies–Cotton design, and each is instrumented with a 499 photomultiplier tube camera providing a field of view of 3°.5. The observatory is sensitive to γ-rays between ∼85 GeV and ∼30 TeV. The angular resolution of the facility is ∼0°.08 at 1 TeV, and its energy resolution is approximately 15% (Holder et al. 2006; Christiansen 2017).

The VERITAS observations of 3C 264 were taken from 2017 February through May, from 2018 February through April, and from 2019 January through May. The AGN was observed for 30-minute runs in "wobble mode," where the source position was offset from the center of the camera field of view by 0°.5 in each of the cardinal directions in successive runs (Fomin et al. 1994). Generally, several runs were taken on each of the individual nights during the approximately monthly "dark periods" in the three seasons of data taking. However, the observed signal from 3C 264 is relatively weak, and therefore results are only reported for coarse temporal bins. A total of 11.0, 47.7, and 12.8 hr of data were taken in weather conditions classified as good quality by VERITAS observers in 2017, 2018, and 2019, respectively. These data are further quality selected based on information from atmospheric-monitoring instruments and the functionality of various subsystems.

The data are reduced using the image-template method (ITM; Christiansen 2017). The point-spread function (PSF) in this analysis is reduced from prior publications owing to the improved angular resolution of the ITM γ-ray reconstruction. The event-selection criterion for identifying γ-ray images and removing background cosmic-ray images is optimized for hard-spectrum sources using Crab Nebula data scaled to 1% of its nominal strength. The signal is extracted from a circular region of 0°.0707 radius centered on the International Celestial
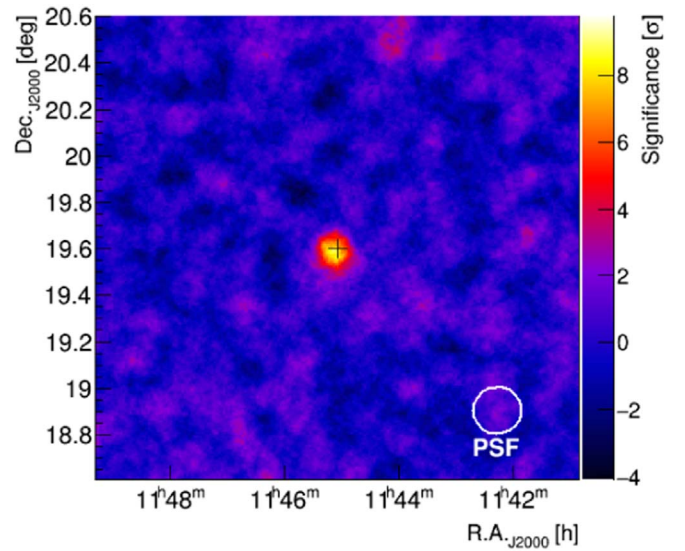

Figure 1. VERITAS sky map of the significance observed from the direction of 3C 264 during 2018. The centroid of the excess observed by VERITAS is within 2σ of the SIMBAD position of 3C 264 (black plus sign). The extent of the VHE source is consistent with the VERITAS point-spread function (PSF). The PSF in this analysis is reduced from prior publications owing to the use of the ITM γ-ray reconstruction (Christiansen 2017).

Reference Frame (ICRF) radio position of 3C 264, and the background is typically determined from 15 off-source regions with the same offset from the center of the VERITAS camera (reflected region method; Berge et al. 2007). The significance of any excess is calculated following Equation (17) of Li & Ma (1983). The γ-ray selection requirements result in an average energy threshold of about 315 GeV for the conditions under which 3C 264 was observed.

Table 1 shows the results from the VERITAS observations. Overall, an excess of 101 γ-ray-like events is observed from the direction of 3C 264, corresponding to a statistical significance of 7.8 standard deviations (σ) above background. While some excess is observed in both the 2017 and 2019 data sets, it is clear that a majority of the signal comes from the 2018 observations, and from 2018 February to March in particular. The 2018 observations yield an excess of 87 events (7.9σ) in 37.9 hr of live time, and the VERITAS results from these data are emphasized in this paper. Figure 1 shows the significance
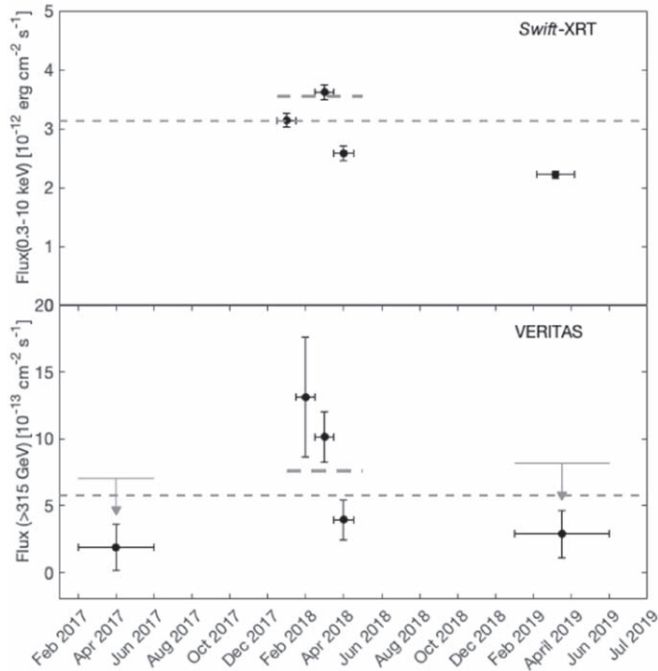
Figure 2. Bottom: VHE light curve measured by VERITAS. The flux was elevated in 2018 February and March. Upper limits at the 99% CL are also shown for the 2017 and 2019 observations owing to the low significance of the observed excesses. The flux observed in 2017−2019 is indicated by the short-dashed line. The 2018 flux is indicated by the dashed line segment. Top: X-ray flux light curve measured by Swift-XRT. The average flux from 2018 to 2019 is indicated by a dashed line.

map for the 2018 data. A clear point source is seen at the position of 3C 264.

The VHE light curve from 3C 264 is shown in Figure 2, and all the plotted integral flux values above the observation threshold of 315 GeV are given in Table 1. The systematic error on the flux measured by VERITAS is 30%. The flux for the total 2017−2019 measurement is shown as a short-dashed line in Figure 2. There is evidence for variability in the annual measurements. A fit of a constant to the annual flux values is poor ($\chi^2 = 9.7$, 2 degrees of freedom, $P(\chi^2) = 0.0079$). This is driven by the elevated flux seen in 2018, $F(>315 \text{ GeV}) = (7.6 \pm 1.2) \times 10^{-13} \text{ cm}^{-2} \text{ s}^{-1}$, which corresponds to 0.7% of the Crab Nebula flux (Albert et al. 2008). Although an elevated flux is seen from 3C 264 in 2018, the observed value places it among the dimmest sources detected in the VHE band. The monthly fluxes observed in 2018 also show evidence for VHE variability, as a similar fit of a constant is poor ($\chi^2 = 8.8$, 2 degrees of freedom, $P(\chi^2) = 0.012$). The poor χ^2 comes from the factor of 2−3 decrease in 2018 April from the elevated flux state observed during the 2018 February to March time period. The significance of the excess observed from 3C 264 in 2017 and 2019 is low during each of those seasons. Correspondingly, 99% confidence level upper limits of $F(>315 \text{ GeV}) < 7.0 \times 10^{-13} \text{ cm}^{-2} \text{ s}^{-1}$ for 2017 and $F(>315 \text{ GeV}) < 8.2 \times 10^{-13} \text{ cm}^{-2} \text{ s}^{-1}$ for 2019 are also reported.

The photon spectrum from the 2018 VERITAS observations of 3C 264 is shown in Figure 3. The data are well fit by a power law of the form $dN/dE \sim E^{-\Gamma}$ ($\chi^2 = 3.0$, 4 degrees of freedom) with a hard photon index of $2.20 \pm 0.27_{\text{stat}} \pm 0.20_{\text{syst}}$ and differential flux normalization of $(1.94 \pm 0.35_{\text{stat}} \pm 0.58_{\text{syst}}) \times 10^{-13} \text{ cm}^{-2} \text{ s}^{-1} \text{ TeV}^{-1}$ at 1 TeV.
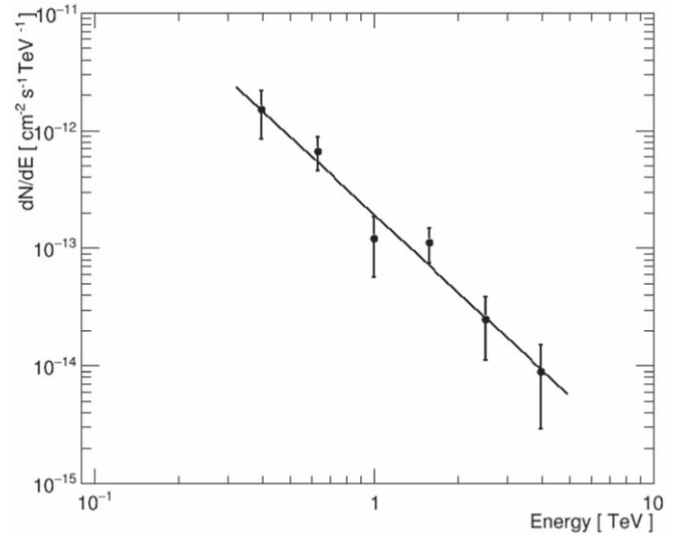
Figure 3. VHE spectrum observed by VERITAS in 2018.

The location of the VERITAS excess is determined using a 2D Gaussian fit to a map of the excess of events. The centroid of the point-like excess is located (J2000) at R.A. $11^h 45^m 8^s.4 \pm 0.7^s_{\text{stat}}$ and decl. (δ) $+19°36'29'' \pm 17''_{\text{stat}}$. The source is accordingly named VER J1145 + 196, and it is located $0°.017$ from the (ICRF) radio position of 3C 264 of R.A. $= 11^h 45^m 05^s.00903$ and $\delta = +19°36'22''.7414$ (Fey et al. 2004). The VERITAS measurement has a systematic uncertainty of $0°.007$ (25''), in addition to the statistical uncertainty of $0°.006$. The systematic uncertainty comes largely from the accuracy of the calibration of the VERITAS pointing system, which corrects for the flexing of each telescope's optical support structure (Griffiths 2015). The reconstructed source position is therefore consistent with the ICRF location at the 2σ level.

3. Multiwavelength Data Sets

3.1. HE γ-Ray Observations

The Fermi Large Area Telescope (LAT) is sensitive to γ-rays from ∼20 MeV to ∼300 GeV, and it operates primarily in a survey mode that covers virtually the entire sky every few hours. 3C 264 appears in several Fermi-LAT catalogs and is associated with the source 4FGL J1144.9+1937. It is not classified as variable in the 8 yr Fermi catalog (Abdollahi et al. 2020), where its spectrum is characterized by a power law with a photon index of 1.94 ± 0.10. Although the object is not listed as a variable source, archival Fermi-LAT observations in the region of 3C 264 were analyzed for the time period coincident with the VERITAS observations in 2018 (2018 February 9 to 2018 April 21), corresponding to mission-elapsed time 539827205 to 545961605, in order to probe the HE emission. A standard "unbinned" likelihood analysis was performed using the Python-based Fermi tools (ver. 1.0.1). In particular, a region of interest (ROI) of 15° around the position of 3C 264 was analyzed including photons with energies from 100 MeV to 100 GeV. The initial maximum likelihood optimization used a model file populated from the 3FGL catalog (Acero et al. 2015). A converged fit was found after some iteration that required both adding new sources to the model file based on residual significance in the "TS" (test statistic) maps and removing some low-significance sources from the 3FGL list.

Table 2
Swift-XRT Spectral Fit Results For 3C 264

Data Set	Normalization (10^{-4} photons cm^{-2} s^{-1} keV^{-1})	Γ	χ^2/dof	0.3-10 keV Model Flux (10^{-12} erg cm^{-2} s^{-1})	ObsID 000105120nn
2018 Jan	6.54 ± 0.25	2.17 ± 0.06	317/486	3.14 ± 0.12	01-04
2018 Mar	7.09 ± 0.26	2.06 ± 0.06	232/408	3.62 ± 0.13	06-09,11-12
2018 Apr	5.42 ± 0.27	2.19 ± 0.08	236/326	2.58 ± 0.13	14,16-21
All 2018	7.15 ± 0.16	2.10 ± 0.04	461/617	3.55 ± 0.08	all of the above
All 2019	4.68 ± 0.13	2.20 ± 0.05	327/598	2.22 ± 0.06	22-27,29-33
2018 + 2019	6.34 ± 0.12	2.12 ± 0.03	487/549	3.13 ± 0.06	all of the above

Note. The normalization and photon index (Γ) are the best-fit results for a power law from `phabs*powerlaw` with $n_H = 1.96 \times 10^{20}$ cm^{-2}. All ObsIDs have the prefix of 000105120.

After the final XML source model file was generated, we used maximum likelihood to measure the flux and spectral index of 3C 264 during the 2018 VERITAS observations. The spectral index has a large error, so we also ran a fit with the spectral index fixed to the 4FGL catalog value, and this source flux is reported in Section 4.1. We also generated a 95% upper limit for the time frame of the 2017 observations using the default method of likelihood profile fitting with the Fermi Upper-Limit tool.

3.2. X-Ray Observations

Swift.—The X-ray Telescope (XRT) aboard the Neil Gehrels Swift Observatory observed 3C 264 (Target ID: 10512) in 2018 and 2019 for a total exposure of 54 ks. The data are almost evenly split between the two years, and these are all known XRT exposures of 3C 264 prior to the end of the VERITAS observations in 2019. These observations were made under several target of opportunity requests, and the observation IDs are listed in Table 2 next to the appropriate spectral fits. Since 3C 264 has a relatively low XRT count rate, all exposures were taken in photon counting (PC) mode. The average count rate is 0.09 counts s^{-1}, well below the suggested threshold of 0.5 counts s^{-1} for performing any pileup correction. All XRT exposures were processed and analyzed with HEASoft V6.26.1.[32] All level-2 data products were created locally using `xrtpipeline` V0.13.5. The spectra were extracted using `XSELECT` V2.4g, and model fitting was performed using `XSPEC` 12.10.1f (via `PyXspec`). The source region is a circle of radius $r = 20$ pixels (about $45''$), while the background region has the same shape and size and was placed nearby to avoid the single other point source in the region.

Each XRT observation was analyzed individually, as well as grouped into the several epochs shown in Table 2. A similar analysis was performed on each sample. Events were extracted between 0.3 and 10 keV. However, due to the relatively weak source, the energy bins above 7 keV are consistent with zero flux in many cases, so model fitting was performed to obtain a flux extrapolated to 10 keV. Each spectrum was fit to a simple absorbed power law using the xspec model `phabs*powerlaw`. The hydrogen column density was fixed at $n_H = 1.96 \times 10^{20}$ cm^{-2}, and the remaining fit (power-law) parameters were left free. This value of n_H was determined using the `nhtot` webtool,[33] which facilitates the use of column density measurements described in Willingale et al. (2013). Since the

source is a point source, the weighted n_H value was used. Past analyses with Chandra and XMM (e.g., Evans et al. 2006; Perlman et al. 2010) found that power-law models provided the best fits for 3C 264 over those including some sort of thermal component (e.g., including xspec models `apec` or `bbody` to the absorbed model). This is also supported by the X-ray emission being possibly dominated by the large-scale jet, and not the core or galactic dust (see Section 4.4). Therefore, no thermal model was included.

Chandra.—3C 264 was observed on 2018 April 4 with the High Resolution Camera (HRC) on board Chandra under Director's Discretionary Time proposal 21058. The exposure time is 14.58 ks, and all data analysis is conducted with CIAO version 4.11. The data are reprocessed in the standard way using the `chandra_repro` script. The total flux from 3C 264 is estimated using the `srcflux` script with the "wide" band appropriate for HRC. Previous Chandra observations of 3C 264 were made using the Advanced CCD Imaging Spectrometer (ACIS), where elongation of the source along the radio/optical jet direction was noted (Perlman et al. 2010). To evaluate the extended emission in the 2018 HRC observations, the Chandra/HRC PSF at the location of 3C 264 was calculated using the online `CHaRT` tool and simulations from CIAO task `psf_project_ray`. To reduce the statistical uncertainty (noise) in the PSF, which is matched to the data by total counts per exposure, 50 realizations of the instrument PSF from `CHaRT` were requested, and the resulting detector-plane PSFs produced by `psf_project_ray` were averaged. This PSF is used to deconvolve the image using the Lucy–Richardson algorithm as implemented in the CIAO task `arestore`.

3.3. Optical Observations

Ground-based.—3C 264 was observed by two ground-based optical observatories as part of a target of opportunity campaign in 2018. Individual Johnson *R*-band exposures were taken on eight nights between 2018 March 22 and 2018 April 10 (MJD 58199−58218) at the 1.3 m Robotically Controlled Telescope (RCT) at Kitt Peak National Observatory. In addition, Johnson *V*-band exposures were acquired on 14 nights between 2018 March 21 and May 20 (MJD 58198-58258) with nearly half of the data each from two nodes of iTelescope.net: the T21-413mm Reflector of the New Mexico Observatory, the T27-770 mm Reflector of the Siding Spring Observatory, and an additional data point was taken with the T32-413 mm Reflector at the Siding Spring Observatory. The data were bias subtracted and flat-field corrected using standard IRAF routines for the RCT observations and MIRA PRO UE

---

[32] https://heasarc.gsfc.nasa.gov/docs/software/heasoft/
[33] https://www.swift.ac.uk/analysis/nhtot/index.php

for the iTelescope.net observations. *V* and *R* magnitudes were determined using differential aperture photometry with a comparison star in the same field of view as 3C 264 and a photometric radius of $10\overset{''}{.}15$.

UVOT.—The Ultraviolet/Optical Telescope (UVOT) aboard Swift observed 3C 264 simultaneously during the XRT exposures described in Section 3.2 (see Table 2). Observations were made using all six filters available (*v, b, u, uvw1, uvm2, uvw2*), and the UVOT exposures were processed using `uvotproduct` version 2.4 to calculate the flux and generate light curves. A circle of radius $r = 5''$ was used for the source. The background was extracted from a nearby, source-free, circle of radius $r = 20''$.

Hubble Space Telescope (HST).—The kiloparsec-scale jet of 3C 264 is visible in the optical, as well as the radio, and has been extensively observed by HST. The recent discovery of optical superluminal proper motions and colliding knots in the jet (Meyer et al. 2015) was enabled by comparing a moderately deep ACS/WFC F606W image[34] in 2014 May against earlier short WFPC2 observations from 1994, 1996, and 2002. Based on this result, a long-term monitoring campaign with HST began in 2015. This campaign has an approximately 2 yr cadence following the 2014 observation; new observations were made in 2015/2016 and 2018/2019. These include polarization imaging with ACS/WFC in F606W and multiband imaging with WFC3/UVIS for diagnostics on possible changes in the knot spectrum as the collision of knots B and C continues. Further details are in E. T. Meyer et al. (2020, in preparation).

3.4. Radio Observations

VLA.—The jet of 3C 264 was observed by the VLA in *K*-band, A-configuration on 2015 August 13 and 2018 April 2. The 2015 observation (Project 15A-507) was taken in order to provide an updated image of the jet after the discovery of the fast proper motion of two of the four knots in the optical. The 2018 April observation was obtained from Director's Discretionary Time (Project 18A-464) in response to the increased VERITAS flux observed in early 2018. The setup and length of these observations were identical. Therefore, the 2015 epoch is an excellent reference to determine whether any changes in the core or jet knots occurred during the VERITAS flare. The data can also be compared to deep *K*-band imaging acquired in 1983 and 2003.

Both recent data sets were calibrated using the `CASA pipeline (version 4.7.2)`, and the scans on 3C 264 were split off for imaging using `clean`. Due to the wide-band observing mode (18–25 GHz), nterms = 2 was used in `clean`. Full polarization products were obtained after several initial rounds of self-calibration. Briggs weighting with a robust parameter of 0.5 was used for all imaging. The pixel scale was set to $0\overset{''}{.}025$ to match the HST imaging scale. The final synthesized beam has a size of $0\overset{''}{.}12 \times 0\overset{''}{.}08$ and $0\overset{''}{.}18 \times 0\overset{''}{.}08$ in the 2015 and 2018 images, respectively. The fractional polarization and electric-vector position angle (EVPA) were calculated according to the standard formulae from the Stokes images.

VLBI.—Observations with the Very Long Baseline Array (VLBA) were made on 2018 March 30 under a Director's Discretionary Time request related to the VHE flaring activity (Project Code BM 450). Simultaneous multifrequency VLBA observations were performed for a total of 4 hr at 5.0 GHz, 8.4 GHz, 12.1 GHz, and 15.3 GHz. Both circular and cross-hand polarizations were recorded with 2-bit sampling at 2048 Mbps, with eight intermediate frequencies, each of 32 MHz bandwidth. The Los Alamos antenna did not participate owing to a telecommunications problem, but useful data were obtained with the other nine VLBA antennas. The frequency scans were interleaved and interspersed with scans on the bright fringe calibrator source OM 280. The total integration times were adjusted to yield an rms image noise of $\sim$0.1 mJy beam^{-1} at each frequency.

Each frequency band was processed following standard procedures in `AIPS` and `DIFMAP` and produced naturally-weighted images with a pixel size of 0.05 mas. The antenna polarization leakage terms were corrected using the `AIPS` task `LPCAL`. It is not possible to calibrate the instrumental polarization EVPA offset owing to a lack of a simultaneous single-dish observation of either 3C 264 or OM 280. Neither source has any jet features with stable EVPA that could be used for calibration purposes.

3C 264 is also monitored as a part of the MOJAVE[35] program. In addition to the new data obtained in March 2018, MOJAVE monitoring data exist since 2016. The MOJAVE sample also includes an archival 15 GHz observation from 2005. For the analysis methods of the MOJAVE program data, please refer to Lister et al. (2018).

4. Multiwavelength Results

4.1. Fermi Observations

3C 264 (4FGL J1144.9+1937) is not a particularly strong Fermi-LAT source, with an 11.4σ significance detection in the 8 yr catalog. Correspondingly, it should only be weakly detected ($\sim$2σ) in a few-month integration, and it is not classified as variable in the 4FGL catalog. The Fermi-LAT data taken contemporaneous (MJD 58158$-$58229) to the VERITAS sample in 2018 indicate a higher flux $F(1-100 \text{ GeV}) = (7.1 \pm 3.7) \times 10^{-9}$ photons s^{-1} cm^{-2} than the 4FGL catalog value of $(2.85 \pm 0.40) \times 10^{-10}$ photons s^{-1} cm^{-2}. The Fermi-LAT data taken during the main VERITAS observing period in 2018 also indicate a flat MeV$-$GeV spectrum ($\Gamma = 2.1 \pm 0.6$), consistent with the 4FGL value ($\Gamma = 1.94 \pm 0.10$). Both the concurrent sample and 8 yr catalog indicate that the peak of the IC component of the SED is in the GeV band.
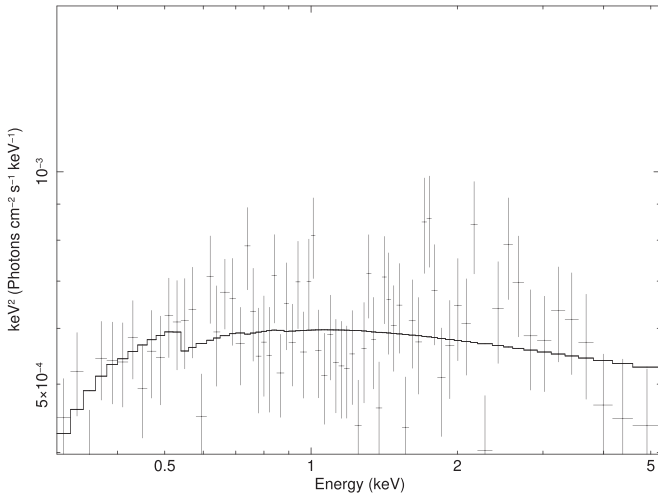
4.2. Swift Observations

The spectral fit results for selected monthly and yearly epochs are shown in Table 2. The χ^2 for each fit is reasonable (i.e., χ^2/dof < 1), and the 2018 + 2019 X-ray spectrum, along with the corresponding fit, is shown in Figure 4 as an example. The monthly binned X-ray flux in 2018 is significantly variable when comparing to the average with χ^2/dof = 32.1/2 (P(χ^2) $\approx 10^{-7}$). Swift did not observe 3C 264 in 2018 February, when VERITAS observed its highest flux, but the general trend is still apparent with the available observations

---

Figure 4. Swift-XRT spectrum and fit for 2018 and 2019.

Figure 5. Deconvolved Chandra HRC-I image of 3C 264 observed on 2018 April 4. The HST image was aligned assuming that the brighter component to the south is the core, and the resulting overlay of the HST contours of the jet is shown. The previously reported thermal emission associated with the host galaxy by Sun et al. (2007) is on the scales of $1.''5-6''$. This image shows very little emission on the same scales (the green circle has a radius of $1.''5$). Color scale is in counts units.

from 2018 January, March, and April. The XRT light curve is shown in Figure 2.

Light curves of the Swift-UVOT exposures were inspected, and no time variability was found. This reinforces the expectation that the emission in this band should be dominated by stars in the galaxy and stable on this timescale. For each UVOT filter, the results were time averaged to find a mean magnitude and energy flux. The results are shown in Table 3.

4.3. Ground-based Optical Observations

No significant variability is found in the light curves from the RCT and iTelescope.net observatories. The largest difference between any two RCT points is 0.06 mag, and no single iTelescope.net point differed by more than 0.16 mag. The mean R-band measurement with RCT is $R = 13.09$, and the mean V-band measurement with iTelescope.net is $V = 13.49$, which correspond to fluxes of 17.9 and 15.4 mJy at 640 and 550 nm, respectively. No attempt is made to subtract the host galaxy flux, and it is important to note that the integration radius for these optical data is ∼2 times larger than that used for the UVOT results.

4.4. Chandra Observations

The deconvolved HRC-I image of 3C 264 is shown in Figure 5, with the HST contours of the jet overlaid. The source is clearly extended in the image. This is also apparent from 2D fitting of the (nondeconvolved) image with sherpa: a double-Sérsic model fits the image best (reduced χ^2 statistic of 0.042), though it leaves a residual extended flux distributed around the source. This fit model is unlikely to be physically meaningful, but the relatively large radii of the Sérsic components (2.2 and 14 pixels) indicate that the bulk of the X-ray emission is extended. A point-source model provides a worse fit (reduced χ^2 statistic of 0.054).

The currently presented observations are the highest-resolution X-ray observations of this system to date. Previous imaging with ACIS-S and XMM suggests an extended thermal component around the AGN arising from the host galaxy on scales of $1.''5-6''$ (0.7–2.6 kpc; Sun et al. 2007), which is considerably larger than the scale of the extended emission shown in Figure 5. Indeed, outside of $1.''5$ the 2018 observation shows very little emission. As the HRC effectively provides no

Table 3
Swift-UVOT Spectral Information, Time Averaged from All 2018−2019 Swift Observations of 3C 264

Filter	Energy Flux (erg cm^{-2} s^{-1})	Magnitude
v	$(3.77 \pm 0.03) \times 10^{-11}$	14.336 ± 0.008
b	$(2.15 \pm 0.02) \times 10^{-11}$	15.305 ± 0.008
u	$(6.87 \pm 0.06) \times 10^{-12}$	15.626 ± 0.009
$uvw1$	$(3.47 \pm 0.04) \times 10^{-12}$	16.192 ± 0.012
$uvm2$	$(2.61 \pm 0.04) \times 10^{-12}$	16.519 ± 0.015
$uvw2$	$(2.49 \pm 0.02) \times 10^{-12}$	16.548 ± 0.010

Note. These measurements cover a significant fraction of the entire galaxy, and not only the core or jet structure.

spectral information, it is difficult to directly assess whether the observed extended emission could be thermal. However, Perlman et al. (2010) took the "core" emission to be everything within $1.''23$ of the peak, which essentially covers the entire region of interest in Figure 5. Their fit to the extracted spectrum showed that a thermal component could contribute no more than 5% of the total flux, with the rest attributed to a nonthermal power-law spectrum with a spectral index $\alpha_x = 1.24$.

Identifying the "core" location in the deconvolved Chandra image of 3C 264 is not unambiguous. This is due to the absolute pointing accuracy of Chandra (90% uncertainty radius is $0.''8$) and HST (typical error is ∼$0.''9$) and the lack of any other source in the HRC field of view. If the brightest pixel is assumed to be the location of the AGN core, then the brightest part of the extended and presumably nonthermal emission would be located to the south and west of the core, which seems unlikely, given that the jet extends to the northwest. Instead, if the bright component shown centered on the HST core in Figure 5 is chosen, then the bulk of the extended emission coincides with the extended optical/radio jet rather

than the core. This is more plausible, though the brightest pixel is offset somewhat to the north side of the jet. If this is indeed the correct identification, then the jet appears to be brighter than the core, which is unusual; the only other case where this has been observed was during the brightest outburst of HST-1 in M87.

Taking the total unabsorbed 0.1–10 keV flux from the 2018 observation of $(6.91 \pm 0.2) \times 10^{-12}$ erg cm^{-2} s^{-1} and adopting the spectral index $\alpha_x = 1.24$ from the previous Perlman et al. (2010) analysis of Chandra/ACIS-S observations taken in 2004 gives a 1 keV monochromatic flux of 0.59 ± 0.02 μJy for the entire region. This is approximately twice as large as the flux $(0.28 \pm 0.1$ μJy) assigned to what was referred to as the core (i.e., a similar region) in the 2004 observation. Crudely separating the extended jet region from the area tentatively identified as the core, we can assign approximately 80% of the flux (470 nJy) to the extended jet. We note that the previously reported flux of 4.6 ± 1.1 nJy for the extended jet in Perlman et al. (2010) was taken for a region outside 0″8 from the core, and thus from a region corresponding to the much fainter/diffuse part of the optical jet, which is not detected in our observations here. The two fluxes are from different regions and should not be compared. It must be emphasized that it is not certain that the core/jet regions are correctly identified in the observations presented here owing to the lack of an absolute astrometric reference. Therefore, only the total X-ray flux is reported in the SEDs presented in Section 5.

4.5. HST Observations

Figure 6 shows images of the radio (VLA) and optical (HST) fractional linear polarization for the large-scale jet in 3C 264 (the VLA radio polarization images are described below in Section 4.6). In the optical, the fractional polarization images were obtained by taking the ratio of the total linear polarization to the galaxy-subtracted Stokes I image; because this subtraction removes the core, the fractional polarization shown in the core region is not meaningful. Indeed, because of the inner dust disk in 3C 264, it is difficult to disentangle the contribution of the galaxy and the synchrotron jet in the core region in the total flux images. However, assuming that all the central flux in the Stokes I image comes from the synchrotron core, it suggests an optical fractional polarization at the core of 16% and 13% in 2016 and 2018, respectively. The integrated optical core luminosity in Stokes I (under a Gaussian fit) rose slightly between 2016 and 2018, from 185 ± 4 μJy to 238 ± 5 μJy.

The large-scale jet shows a much higher level of polarization just downstream of the knot B/C collision zone (Meyer et al. 2015), as shown in Figure 6 (the collision region is indicated with a black line). The linear polarization fraction of this feature does not appear to change significantly between 2016 April and 2018 March, with a value of ∼25%–35% in both epochs when accounting for the contribution to the Stokes I flux from the galaxy. The size and location of this region in the two epochs are found to be consistent at approximately 0″5 (220 pc) from the core and 90 pc in extent (based on a Gaussian fit). The position angle of the magnetic field (shown in Figure 6, 90° rotated from the EVPA) also appears largely consistent between the two epochs. It shows a smooth "flow" pattern aligned with the jet direction, with only a hint of some periodic transverse component. Interestingly, there does appear to be a small region in the center of the knot B/C collision zone

where the B-field direction becomes perpendicular to the flow. This is consistent with the scenario outlined in Meyer et al. (2015), which suggests that the collision is in the incipient stages. There is a possible enhancement of the linear polarization fraction that appears in the 2018 image just downstream of stationary knot A, where the polarization fraction reaches 15% (uncorrected). However, this region is very close to the bright core of the jet, and differences in the orientation of HST during the two observations could change the shape and distribution of features in the Stokes I image near the core, making any features less certain.

Figure 7 shows the ACS/WFC F606W image of the jet taken in 2014, as well as the WFC3/UVIS F814W images acquired in 2015 and 2019. These observations are also useful for comparing the state of the jet before and after the increased VHE flux. The multiband WFC3/UVIS observations taken in 2019 January were taken as replacements for 2018 June observations that missed the jet owing to a problem with a gyroscope on the spacecraft. As shown, very little change can be seen between 2014 and 2019. There is a slight shift of the knot B/C centroid, which is expected based on the previously detected proper motions. The change in core brightness, at 20%–30%, is typical for blazars and moderately well-aligned sources. A further discussion of the kinematics of the jet will be given in a future publication.

4.6. VLA

The VLA observations of 3C 264 have somewhat lower resolution than the HST imaging. However, the polarization structure also shown in Figure 6 appears very similar. Further, there is no obvious change between the observations taken in 2015 and those taken in 2018, during the period of increased VHE flux. The K-band core flux in 2015 was 167 mJy and decreased to 121 mJy in 2018.

4.7. VLBI

After registering the VLBA images, a map of spectral index values α, where $S_\nu \propto \nu^{+\alpha}$, was produced by performing a linear regression on the intensity values S_ν of each pixel. Only pixels that exceeded three times the image noise level at all four frequencies were considered. The spectral morphology map is shown in Figure 8, with contours overlaid from the 5 GHz total-intensity map.

The spectral index values in Figure 8 are only representative of the actual spectrum in regions of the jet where the turnover frequency does not lie between 5.0 and 15.3 GHz. To investigate this further, the self-absorbed synchrotron spectra (see Equation (4) of Hovatta et al. 2014) were fit for each pixel, and the resulting turnover frequency values ν_m are also shown in Figure 8. In this map, ν_m values below ∼6 GHz and above ∼12 GHz are not well constrained by the data. However, some clear trends emerge when comparing the two VLBA maps. The core region has a self-absorbed spectrum peaking at ∼8 GHz, and the jet becomes optically thin roughly 4 mas (13 pc projected) downstream. At 11 mas downstream, there is an isolated jet feature with an inverted spectrum. The high fractional linear polarization at this location (∼15% at 5 GHz) may be indicative of a transverse shock that is accelerating the electrons and enhancing the magnetic field strength perpendicular to the jet.
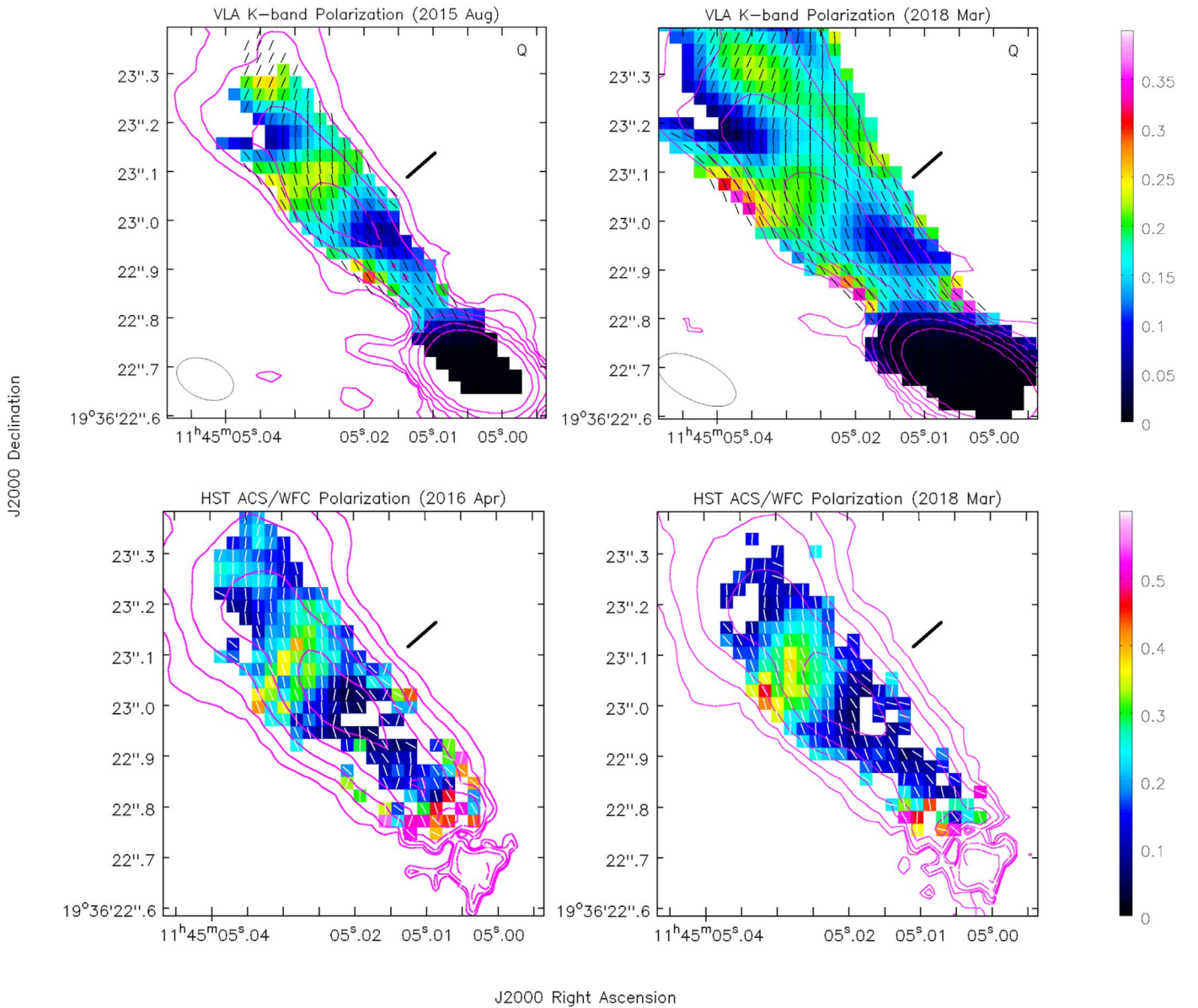
Figure 6. High-resolution radio and optical polarization images of 3C 264 from the VLA and HST. These images all show the fractional linear polarization, on a scale from 0% to 40% in the radio and from 0% to 60% in the optical. The VLA K-band polarization is shown in 2015 August (top left) and 2018 March (top right). There is no striking difference in the level of polarization in the jet, both showing a peak of about 22%–23% polarization just downstream of the knot B/C collision region, indicated by the black line (Meyer et al. 2015). The peak of HST-optical polarization is in the same location and reaches ∼15%–17%. It also shows similar levels in 2016 April (bottom left) and 2018 March (bottom right). The polarization values are uncorrected for the effect of dilution from the light from the galaxy/dust disk. In all images, the vector lines show the direction of the magnetic field (90° rotation from the EVPA), and the contour lines show the flux in the corresponding Stokes I image for each epoch/band. In the radio images, contours are drawn at 1, 2, 4, 8, and 16 times the base level of 5×10^{-4} Jy. In the optical images, the contour lines are drawn at 2, 4, 8, 16, and 32 times the base level of 1×10^{-8} Jy.

The VLBA imaging of the jet is shown in Figure 9. No significant change in either the core or any of the jet features was observed between any epochs taken during the VHE high state.

5. Discussion

5.1. Multiwavelength Observations

The VERITAS observations of 3C 264 in 2017−2019, as shown in Figure 2, indicate a period of enhanced VHE flux lasting at least several weeks in early 2018. This elevated state enabled the relatively quick discovery of the source at VHE and motivated an intensive multiwavelength campaign to

search for the origin of the VHE enhancement. However, there is no clearly identifiable source of the event. In the high-resolution radio and optical imaging from early 2018, there is no evidence of any significant change in the larger-scale jet beyond the core, i.e., no flaring event comparable to the well-known HST-1 flare in M87. The X-ray flux seen in the 2018 Chandra/HRC observation is significantly increased (by a factor of 2) over that detected by Chandra/ACIS in 2005. However, the current Chandra imaging is inconclusive as to the location of this increase owing to both the ambiguity of the core identification and the lack of a prior epoch of similar resolution. The flux observed from the core in other bands does not show a consistent pattern. It actually decreased by 27% in
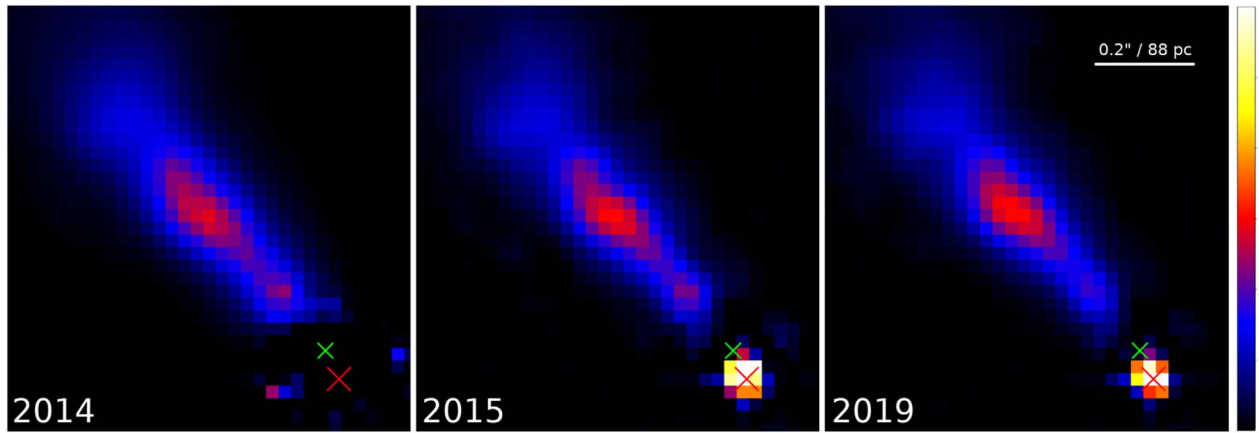
Figure 7. HST images of the kiloparsec-scale jet in 3C 264. In all cases, the light from the galaxy and inner dust disk is modeled and subtracted. The images from 2014 May (left; ACS/WFC F606W), 2015 November (middle; WFC3/UVIS F814W) and 2019 January (right; WFC3/UVIS F814W) are shown. The red cross marks the location of the central black hole, and the green cross marks the location of a bend in the jet seen in VLBA imaging. The color bar scale shown at left is in units of μJy.
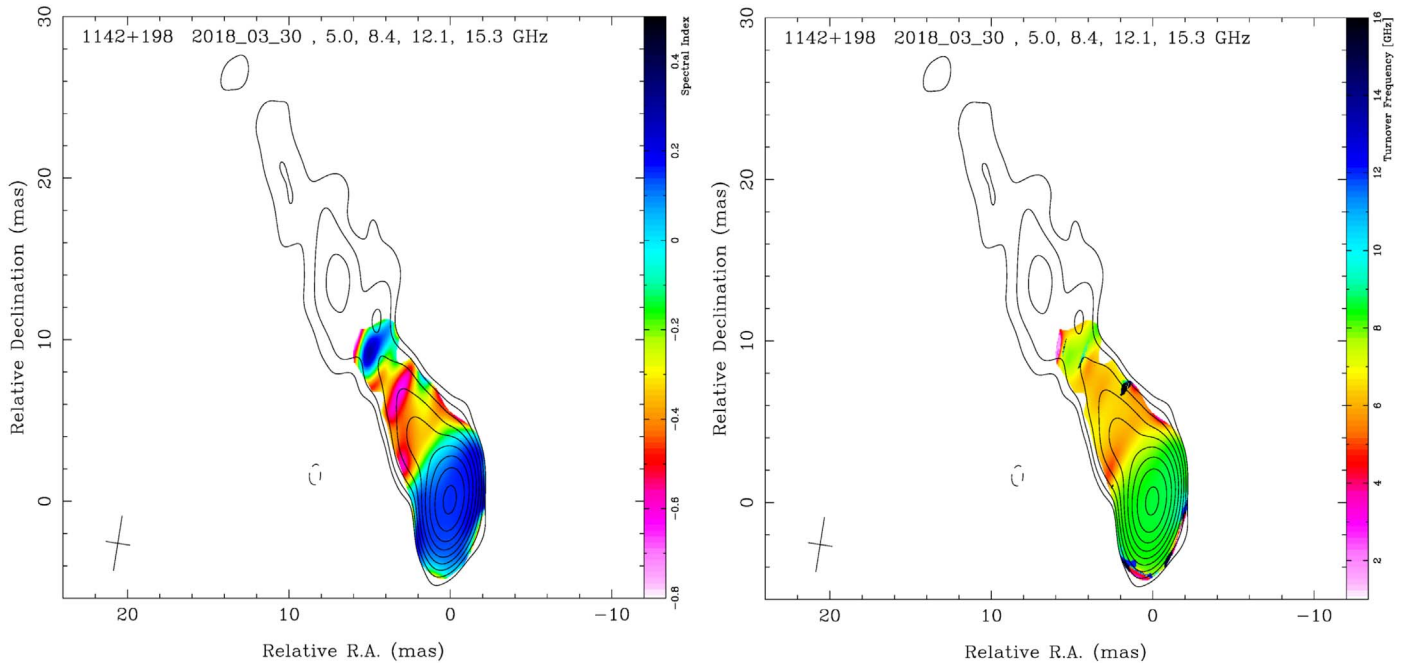
Figure 8. Results from VLBA images of 3C 264 taken at 5.0, 8.4, 12.1, and 15.3 GHz on 2018 March 30. Maps of the radio spectral index (left) and the synchrotron spectral turnover frequency (right) are shown. The VLBA images were restored with a common Gaussian beam having FWHM dimensions 3.4×1.5 mas at position angle $-9°$. The 5.0 GHz total-intensity contours are drawn at successive factors of two times the base contour level of 0.4 mJy beam^{-1}.

the radio band between 2015 August and 2018 April, while it increased by a modest 21% in the V-band optical (F606W filter) over a similar time frame (2016 April to 2018 March). This level of optical variability appears to be typical based on observations of the core at other epochs. For example, there is a 22% drop in flux between the HST F475W observations in 2015 and 2019.

The broadband SED for 3C 264 is shown in Figure 10, including historical core fluxes and the 2018 HST (F606W Stokes I), Chandra, Swift, Fermi, and VERITAS fluxes, as well as the upper limits from γ-ray observations in 2017. What is immediately notable about the core SED is the broadness of the lower-energy synchrotron peak, compared to typical blazars, or even M87. Given that only mild (factor of 2–3) variations are seen in the 3 yr VERITAS data set, and that the Fermi-LAT flux in 2018 is only marginally higher than the 8 yr average flux

reported in the 4FGL catalog, it seems likely that the enhanced flux observed by VERITAS in 2018 was related not to an extreme flare (i.e., an event with 10–20× higher flux than normal) but to a modestly elevated state.

Using a self-consistent synchrotron and SSC model (dashed and solid lines in Figure 10), we are able to reasonably reproduce the observed SED. The modeling code is based on Graff et al. (2008). It takes an injected electron distribution and uses a kinetic equation solved forward in time to find a steady-state electron distribution, which is then used to calculate the synchrotron and IC emission. Here we use a Doppler factor of 10, and we inject a power-law electron distribution with an index of 2.6 and electron Lorentz factor confined between 200 and 2×10^6. The comoving injected power is 2×10^{42} erg s^{-1}, the comoving magnetic field is 2×10^{-2} G, and the radius of the source is 2×10^{16} cm. With these choices the source is particle dominated and the radiative
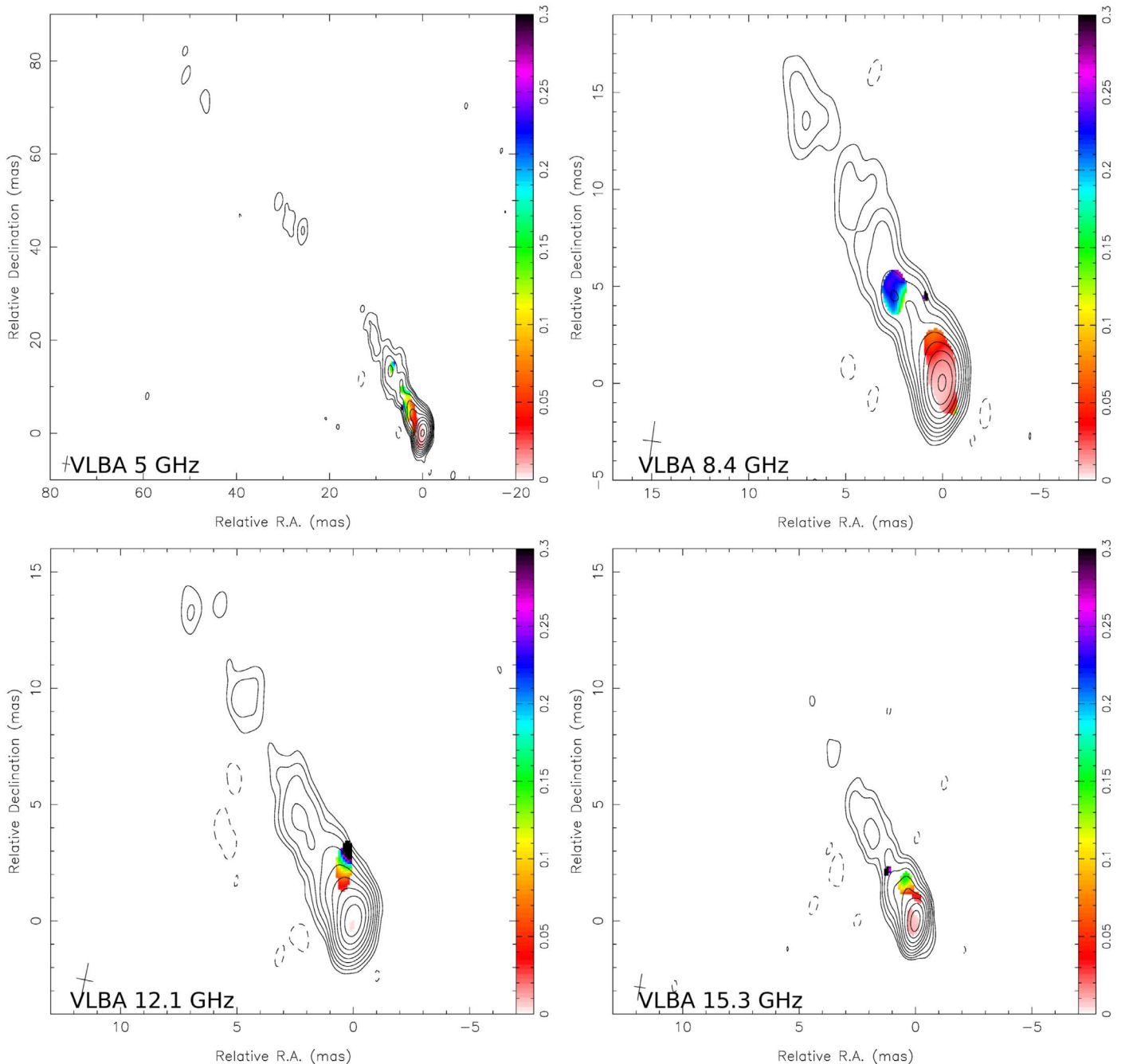
Figure 9. VLBA naturally-weighted contour maps of 3C 264 at 5.0, 8.4, 12.1, and 15.3 GHz. The fractional linear polarization is overlaid in false color for pixels with total linearly polarized intensity above 0.2, 0.45, 0.45, and 0.5 mJy beam^{-1}, respectively. The contours are drawn in successive factors of two times the base contour level of 0.2, 0.25, 0.29, and 0.3 mJy beam^{-1}. A single negative contour equal to the base contour is also drawn using dashed lines. The peak total intensity of the map is 119, 144, 132, and 116 mJy beam^{-1}, respectively. The dimensions and orientation of the restoring beam are indicated by a cross in the lower left corner of each panel. The 5.0 GHz image (top left) is shown on a different, larger scale.

cooling takes place in the slow cooling regime. The model parameters are typical of BL Lac objects, except that the Doppler factor is somewhat lower. The peak is notably at a relatively high frequency, which is unusual for radio galaxies (Meyer et al. 2011). The straight portion of the synchrotron curve is not able to perfectly match the optical/X-ray flux points; this is a limitation of using a single-zone model with a power-law distribution of electron energies—a more complex model (multizone and/or with a log-parabolic energy spectrum) may fit the data better, though at the cost of more input parameters. More complex modeling of this source is left to future work. Based on the single-zone model here,

similar to some other BL Lac objects and radio galaxies, the VHE part of the model is visually softer than the relatively flat slope indicated by the VHE data, suggesting that there is a need for multiple components or more complex models to produce harder VHE emission (see, e.g., the case of AP Librae; Hervet et al. 2015; Zacharias & Wagner 2016; Petropoulou et al. 2017).

5.2. 3C 264 as an M87 Analog

As noted in the introduction, 3C 264 bears some resemblance to M87. They have identical jet powers, exhibit a
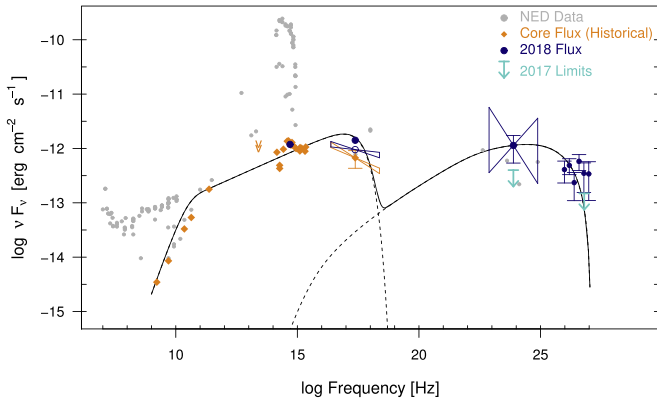
Figure 10. Broadband SED for 3C 264. Gray points are historical fluxes from NED, where the low-frequency radio is dominated by the isotropically emitting radio lobes and the optical by the host galaxy. Shown in orange are the isolated flux values for the core as seen by VLA, ALMA, HST, and Chandra (data taken from NED, this paper, and Perlman et al. 2010). At high energies two temporal states are shown for 3C 264. The cyan upper limits at GeV energies and VHE correspond to the upper limits in 2017 from Fermi-LAT and VERITAS, while the dark-blue data points and Fermi spectrum show the measurements from the 2018 enhanced state. We also show the contemporaneous optical and X-ray fluxes from 2018 as dark blue circles; in the X-rays this includes the Chandra total measurement (filled point, no spectrum) and the VERITAS-concurrent Swift measurement (open point with butterfly spectrum). The model shown (dashed and solid lines) is a self-consistent synchrotron + SSC model with parameters typical of BL Lac objects.

Figure 11. SED comparison for the 3C 264 nonthermal emission in 2018 (red) and M87 (light blue). The low-energy data points for both objects come from high-resolution imaging where the core flux can be isolated from other emission, while the HE (Fermi-LAT) and VHE data are for the total source. For M87, the data and fit are taken from the "average" state SED of de Jong et al. (2015), Figure 3. The model curve for 3C 264 is the same as in Figure 10. While both objects have remarkably consistent radio spectra, 3C 264 clearly has a much higher synchrotron peak, near or at the X-rays, where it is also nearly 50 times more luminous than M87. Similarly, the HE and VHE luminosity of 3C 264 is also clearly higher than M87.

one-sided optical jet with multiple knots, and are the only objects with optical superluminal jets on kiloparsec scales. Each has a stationary knot feature that is the first bright optical knot in the jet, located at about 100 pc (projected) from the core (knot HST-1 in M87 and knot A in 3C 264). Following this, both show fast superluminal motion up to $5c$–$7c$ in the following knots, with speeds decreasing along the jet (Meyer et al. 2013, 2015). The main difference is that the optical jet of 3C 264 is about one-quarter the length of M87. This could be in part due to increased foreshortening due to a smaller orientation angle for 3C 264, although 3C 264 also has fewer optical knots than M87 (4 vs. ~7). Note that the observed optical proper motions set the maximum angle of each jet to similar values (16° and 19° for 3C 264 and M87, respectively[36]), but this does not necessarily mean that they actually have similar orientation angles or intrinsic (as opposed to observed) speeds.

The comparison between 3C 264 and M87 is particularly interesting in light of the currently presented VHE detection because of the HE flaring behavior observed in M87 in the 2000s. These M87 observations consist of two distinct sets. First, Chandra observed dramatic X-ray variability from knot HST-1 in M87 (100 pc from the core, projected), where the flux increased by a factor of 50 over 5 yr (Harris et al. 2006), peaking in mid-2005. The dramatic increase was also seen at radio and optical wavelengths. In both the optical and X-rays, HST-1 actually outshone the core during the flare (Perlman et al. 2003). The knot also showed considerable shorter-timescale variability on the order of 20 days (Harris et al. 2009).

Second, during the same decade, three major VHE flares were observed from M87 in 2005 April, 2008 February, and 2010 April (Aharonian et al. 2006; Acciari et al. 2009; Aliu et al. 2012), each with day-scale VHE variations. There has

been considerable speculation about the location of these VHE flaring events. While typically it is assumed that only the core region would be compact enough to give rise to the day-scale VHE variability, the extreme X-ray outburst of the HST-1 knot led some to consider it as an alternative site (Stawarz et al. 2006; Cheung et al. 2007; Harris et al. 2009, 2012). Confirming any VHE flare arising hundreds of parsecs or more downstream of the base of the jet would be a major discovery and would significantly challenge models of jet formation, especially given the required small emission regions. However, high-resolution imaging conducted at the time of the 2008 and 2010 flares seems to point to the core and not the HST-1 knot as being the source of the VHE flaring in M87 (Abramowski et al. 2012). This is based on increased core activity during these VHE flares (see also Georganopoulos et al. 2005). While those authors make a convincing case for a "blazar-like" origin for the VHE emission in M87 (during both quiescent and flaring states), the VHE emission has never been conclusively shown to originate in the core or HST-1. The possibility of more than one location is also not disfavored by the data (Abramowski et al. 2012).

In light of the many points of similarity already noted between 3C 264 and M87, it is interesting to compare the broadband SEDs directly. The VHE flux of M87 at its peak brightness during the 2010 flare reached ~10% Crab (Aliu et al. 2012). At the distance of 3C 264 this is equivalent to 0.5% Crab, remarkably similar to the flux detected from 3C 264 in 2018 (0.7% Crab). A direct comparison of the SEDs for the M87 core to that of 3C 264 is shown in Figure 11. The data for M87 are taken from de Jong et al. (2015) and represent an average state for the source, while the data and models for 3C 264 are the same as in Figure 10. Here for both sources the isolated core measurements are used from radio to X-rays, while total luminosity results (presumed to be dominated by the core) are reported at HE and VHE. It is interesting that the radio portions of the SEDs of 3C 264 and M87 are practically identical but then deviate from each other at frequencies above ~10^{13} Hz. The 3C 264 synchrotron spectrum peaks somewhere between the optical and the X-rays, and the M87 synchrotron
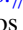
spectrum peaks somewhere around $\sim 10^{13}-10^{14}$ Hz. The HE SED of 3C 264 is about 10 times brighter than that of M87. This behavior can be explained in the context of models with velocity profiles, such as a decelerating flow (Georganopoulos & Kazanas 2003) or a fast-spine, slow-sheath jet (Ghisellini et al. 2005), where the two jets are physically similar but have different orientations, with 3C 264 being closer to the line of sight than M87. In such a scenario, where the HE electrons produce the optical to X-ray synchrotron emission and the γ-ray IC emission comes from the faster parts of the flow, misaligning the jet causes the more highly beamed emission to correspondingly drop faster as the jet moves away from the observer. Qualitatively, this would produce something like the observed differences between the two SEDs in Figure 11. Detailed modeling work to test this scenario will be considered in a future publication.

6. Summary

VHE γ-ray emission was discovered from the radio galaxy 3C 264 by VERITAS in the spring of 2018. This AGN is the most distant radio galaxy detected in the VHE to date, and the discovery was facilitated by a period of enhanced VHE flux lasting for several weeks. An extensive suite of contemporaneous multiwavelength observations was acquired to probe the underlying emission mechanism. These include high-resolution observations with the VLBA, VLA, HST, and Chandra, as well as observations by Swift in the optical and X-ray, γ-rays by the Fermi-LAT, and ground-based optical observations. The mild VHE variability observed by VERITAS in 2017–2019 suggests that 3C 264 did not experience a strong flare, but rather a period of modestly enhanced flux. The source of this enhanced flux is most likely the unresolved core, based on the lack of any notable change in any of the high-resolution Chandra or HST imaging compared with previous epochs spanning the previous decade; we also did not observe any large changes in the core flux at lower frequencies. A qualitative inspection of the SED for the jet of 3C 264 shows that it is somewhat unusual for a radio galaxy, with a relatively high frequency synchrotron peak near the X-rays. 3C 264 could be considered a more distant analog of the well-studied VHE source M87 based on both its beamed and unbeamed radio emission and its kinematic profile. If it is intrinsically similar, then 3C 264 is likely oriented at a smaller angle to the line-of-sight.

ORCID iDs

W. Benbow ⓘ https://orcid.org/0000-0003-2098-170X
R. Bird ⓘ https://orcid.org/0000-0002-4596-8563
J. L. Christiansen ⓘ https://orcid.org/0000-0002-8035-4778
M. Errando ⓘ https://orcid.org/0000-0002-1853-863X
Q. Feng ⓘ https://orcid.org/0000-0001-6674-4238
P. Fortin ⓘ https://orcid.org/0000-0001-8963-4437
L. Fortson ⓘ https://orcid.org/0000-0002-1067-8558
A. Furniss ⓘ https://orcid.org/0000-0003-1614-1273
M. Georganopoulos ⓘ https://orcid.org/0000-0002-2040-8666
G. H. Gillanders ⓘ https://orcid.org/0000-0001-8763-6252
D. Hanna ⓘ https://orcid.org/0000-0002-8513-5603
O. Hervet ⓘ https://orcid.org/0000-0003-3878-1677
P. Kaaret ⓘ https://orcid.org/0000-0002-3638-0637
D. Kieda ⓘ https://orcid.org/0000-0003-4785-0101
M. L. Lister ⓘ https://orcid.org/0000-0003-1315-3412
G. Maier ⓘ https://orcid.org/0000-0001-9868-4700
E. Meyer ⓘ https://orcid.org/0000-0002-7676-9962
R. Mukherjee ⓘ https://orcid.org/0000-0002-3223-0754
M. Pohl ⓘ https://orcid.org/0000-0001-7861-1707
E. Pueschel ⓘ https://orcid.org/0000-0002-0529-1973
A. Sadun ⓘ https://orcid.org/0000-0001-8086-7242
M. Santander ⓘ https://orcid.org/0000-0001-7297-8217
K. Shahinyan ⓘ https://orcid.org/0000-0001-5128-4160

References

Abdollahi, S., Acero, F., Ackermann, M., et al. 2020, ApJS, 247, 33
Abramowski, A., Acero, F., Aharonian, F., et al. 2012, ApJ, 746, 151
Acciari, V. A., Aliu, E., Aune, T., et al. 2009, ApJ, 707, 612
Acero, F., Ackermann, M., Ajello, M., et al. 2015, ApJS, 218, 23
Aharonian, F., Akhperjanian, A. G., Anton, G., et al. 2009, ApJL, 695, L40
Aharonian, F., Akhperjanian, A. G., Bazer-Bachi, A. R., et al. 2006, Sci, 314, 1424
Aharonian, F. A. 2000, NewA, 5, 377
Albert, J., Aliu, E., Anderhub, H., et al. 2008, ApJ, 674, 1037
Aleksić, J., Antonelli, L. A., Antoranz, P., et al. 2014, A&A, 563, A91
Aliu, E., Arlen, T., Aune, T., et al. 2012, ApJ, 746, 141
Arsioli, B., & Chang, Y. L. 2018, A&A, 616, A63
Barkov, M. V., Bosch-Ramon, V., & Aharonian, F. A. 2012, ApJ, 755, 170
Berge, D., Funk, S., & Hinton, J. 2007, A&A, 466, 1219
Biretta, J. A., Sparks, W. B., & Macchetto, F. 1999, ApJ, 520, 621
Blakeslee, J. P., Jordán, A., Mei, S., et al. 2009, ApJ, 694, 556
Błażejowski, M., Sikora, M., Moderski, R., & Madejski, G. M. 2000, ApJ, 545, 107
Böttcher, M. 2007, Ap&SS, 309, 95
Cheung, C. C., Harris, D. E., & Stawarz, Ł. 2007, ApJL, 663, L65
Christiansen, J. 2017, ICRC (Busan), 35, 789
de Jong, S., Beckmann, V., Soldi, S., Tramacere, A., & Gros, A. 2015, MNRAS, 450, 4333
Dermer, C. D., Schlickeiser, R., & Mastichiadis, A. 1992, A&A, 256, L27
Evans, D. A., Worrall, D. M., Hardcastle, M. J., Kraft, R. P., & Birkinshaw, M. 2006, ApJ, 642, 96
Fanaroff, B. L., & Riley, J. M. 1974, MNRAS, 167, 31P
Feretti, L., Giovannini, G., Klein, U., et al. 1998, A&A, 331, 475
Fey, A. L., Ma, C., Arias, E. F., et al. 2004, AJ, 127, 3587
Fomin, V. P., Stepanian, A. A., Lamb, R. C., et al. 1994, APh, 2, 137
Fraija, N., Marinelli, A., Galván-Gámez, A., & Aguilar-Ruiz, E. 2017, APh, 89, 14
Georganopoulos, M., & Kazanas, D. 2003, ApJL, 594, L27
Georganopoulos, M., Perlman, E. S., & Kazanas, D. 2005, ApJL, 634, L33
Ghisellini, G., Tavecchio, F., & Chiaberge, M. 2005, A&A, 432, 401
Graff, P. B., Georganopoulos, M., Perlman, E. S., & Kazanas, D. 2008, ApJ, 689, 68
Griffiths, S. T. 2015, PhD thesis, Univ. Iowa
Harris, D. E., Beilicke, M., Cheung, C. C., et al. 2012, IJMPS, 8, 348
Harris, D. E., Cheung, C. C., Biretta, J. A., et al. 2006, ApJ, 640, 211
Harris, D. E., Cheung, C. C., Stawarz, Ł., Biretta, J. A., & Perlman, E. S. 2009, ApJ, 699, 305
Harris, G. L. H., Rejkuba, M., & Harris, W. E. 2010, PASA, 27, 457

Hervet, O., Boisson, C., & Sol, H. 2015, A&A, 578, A69
HESS Collaboration, Abdalla, H., Abramowski, A., et al. 2018, MNRAS, 476, 4187
Holder, J., Atkins, R. W., Badran, H. M., et al. 2006, APh, 25, 391
Hovatta, T., Aller, M. F., Aller, H. D., et al. 2014, AJ, 147, 143
Kadler, M., Eisenacher, D., Ros, E., et al. 2012, A&A, 538, L1
Li, T. P., & Ma, Y. Q. 1983, ApJ, 272, 317
Lister, M. L., Aller, M. F., Aller, H. D., et al. 2018, ApJS, 234, 12
Meyer, E. T., Fossati, G., Georganopoulos, M., & Lister, M. L. 2011, ApJ, 740, 98
Meyer, E. T., Fossati, G., Georganopoulos, M., & Lister, M. L. 2012, ApJL, 752, L4
Meyer, E. T., Georganopoulos, M., Sparks, W. B., et al. 2015, Natur, 521, 495
Meyer, E. T., Sparks, W. B., Biretta, J. A., et al. 2013, ApJL, 774, L21
Paggi, A., Massaro, F., Vittorini, V., et al. 2009, A&A, 504, 821
Perlman, E. S., Harris, D. E., Biretta, J. A., Sparks, W. B., & Macchetto, F. D. 2003, ApJL, 599, L65

Perlman, E. S., Padgett, C. A., Georganopoulos, M., et al. 2010, ApJ, 708, 171
Petropoulou, M., Vasilopoulos, G., & Giannios, D. 2017, MNRAS, 464, 2213
Rieger, F., & Levinson, A. 2018, Galax, 6, 116
Sijbring, D., & de Bruyn, A. G. 1998, A&A, 331, 901
Sikora, M., Begelman, M. C., & Rees, M. J. 1994, ApJ, 421, 153
Sikora, M., Stawarz, Ł., Moderski, R., Nalewajko, K., & Madejski, G. M. 2009, ApJ, 704, 38
Stawarz, Ł., Aharonian, F., Kataoka, J., et al. 2006, MNRAS, 370, 981
Sun, M., Jones, C., Forman, W., et al. 2007, ApJ, 657, 197
Tully, R. B., Courtois, H. M., Dolphin, A. E., et al. 2013, AJ, 146, 86
Urry, C. M., & Padovani, P. 1995, PASP, 107, 803
Wakely, S. P., & Horan, D. 2008, ICRC (Mérida), 3, 1341
Willingale, R., Starling, R. L. C., Beardmore, A. P., Tanvir, N. R., & O'Brien, P. T. 2013, MNRAS, 431, 394
Zacharias, M., & Wagner, S. J. 2016, A&A, 588, A110